Wind Energ. Sci., 2, 641–652, 2017
https://doi.org/10.5194/wes-2-641-2017

WIND
ENERGY
SCIENCE
Open Access

Effects of defects in composite wind turbine blades – Part 1: Characterization and mechanical testing

Jared W. Nelson[1], **Trey W. Riddle**[2], **and Douglas S. Cairns**[3]

[1]SUNY New Paltz, Division of Engineering Programs, New Paltz, NY, USA
[2]Sunstrand, LLC, Louisville, KY, USA
[3]Montana State University, Dept. of Mechanical and Industrial Engineering, Bozeman, MT, USA

Correspondence: Jared W. Nelson (nelsonj@newpaltz.edu)

Received: 3 March 2017 – Discussion started: 11 April 2017
Revised: 21 August 2017 – Accepted: 6 November 2017 – Published: 19 December 2017

Abstract. The Montana State University Composite Material Technologies Research Group performed a study to ascertain the effects of defects that often result from the manufacture of composite wind turbine blades. The first step in this multiyear study was to systematically quantify and enter these defects into a database before embedding similar defects into manufactured coupons. Through the Sandia National Laboratories Blade Reliability Collaborative (BRC), it was determined that key defects to investigate were fiber waves and porosity. An inspection of failed commercial-scale wind turbine blades yielded metrics that utilized specific parameters to physically characterize a defect. Methods to easily and consistently discretize, measure, and assess these defects based on the identified parameters were established to allow for statistical analysis. Data relating flaw parameters to frequencies of occurrence were analyzed and found to fit within standard distributions. Additionally, mechanical testing of coupons with flaws based on these physical characterization data was performed to understand effects of these defects. Representative blade materials and manufacturing methods were utilized and both material properties and damage progression were measured. It was observed that flaw parameters directly affected the mechanical response. While the data gathered in this first step are widely useful, it was also intended for use as a foundation for the rest of the study, to perform probabilistic analysis and comparative analysis of progressive damage models.

1 Introduction and background

With the rapid growth of the wind segment of the energy market, it is important that wind farms achieve maximum availability by reducing downtime due to maintenance and failures. Since most components of a wind turbine are located over 60 m (200 ft) above the ground and are large and complex, performing repairs on site is costly and difficult. Repairs to these systems not only require the turbine to be shut down but the problematic system will often require a crane for removal. This is especially true for wind turbine blades for which continuous fiber composite materials have become an optimal choice due to their high strength-to-weight ratio. Lower cost fiberglass materials and manufacturing methods have become the standard for wind turbine blades to compete with traditional energy production technologies. While the resulting final cost can be up to 2 orders of magnitude less than a typical aerospace composite structure, the inclusion of manufacturing defects is more likely. Typical defects are addressed in design using knockdown factors that are often conservative, adding weight, cost, and time. Even with these knockdowns, it has been inferred that design and manufacturing within the wind industry do not always ensure a 20-year design life (Hill et al., 2009). A comprehensive study to characterize and understand the manufacturing flaws common in blades has not been performed within the public domain; however, research has been performed to better understand what is needed to improve blade reliability (Hill et al., 2009; Red, 2008; Walford, 2008; Veldkamp, 2008). The Blade Reliability Collaborative (BRC), led by Sandia National Laboratories and sponsored by the Department of Energy, was formed in large part to address this issue. The research described herein compiles the first stage of a multiyear program performed by Montana State University (MSU) within two areas – flaw characterization and effects of defects.

The primary goal of the MSU research initiative has been to develop a protocol that can be employed in a quality assurance and reliability program to quantify the implications of wind turbine blades containing manufacturing defects to ensure blade life while reducing costly repairs. In turn, these methods may then be used to improve blade manufacturing and design procedures. The function of the flaw characterization portion of this program has been to provide quantitative analysis for two major directives: (i) acquisition and generation of quantitative flaw data describing common defects in composite wind turbine blades and (ii) development of a flaw severity designation system and probabilistic risk management protocol for as-built flawed structures (Riddle et al., 2017). The effects of defects portion focused on the development of state-of-the-art modeling capabilities, correlated to experimental data, to predict the mechanical response of included flaws (Nelson et al., 2017). As such, a foundational work to characterize typical defects and ascertain their effects on mechanical performance was performed and presented herein with both references above as companion papers.

2 Wind industry blade survey and flaw characterization

The BRC directed the MSU team to investigate the effects of porosity and in-plane (IP) and out-of-plane (OP) waves shown in Fig. 1. As a point of distinction, wrinkles, where the wave has a fold-back reversal, were not included in the program. Based on statistical commonality in wind turbine blades, it was critical to the development of this program to identify the precise geometric nature of these flaws. To do this, a field study was performed using several commercial-scale wind turbine blades that had been cut into sections and reviewed for both IP and OP waves in which fibers deviate from ideal longitudinal straightness of the non-woven, unidirectional material. Images of these same sections were also taken for porosity analysis. This data set, while relatively small, provided a strong starting point for the entire project and specifically for the development of a protocol by which other blades may be examined and flaws may be characterized going forward. These techniques are not manufacturer or size dependent, and, in theory, could be applied to any composite structure. While the methods used here are destructive, nondestructive inspection methods to find and quantify these defects continue under the probability of detection activity within the BRC (Roach et al., 2010).

The process by which IP and OP wave data were collected was essentially the same. An image processing software was used on photographs of as-built flawed blade sections in which each defect feature was manually traced with a line as shown in black in Fig. 2a. A separate processing script was written to extract the spatial coordinate data of the traced defect line. From these data, each complete waveform was discretized into separate individual waveforms. One example of a complete wave and the waveform discretization process is shown in Fig. 2.

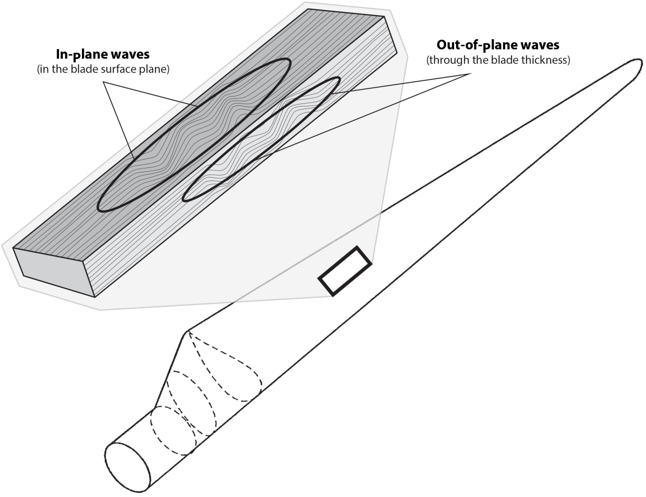

Figure 1. Examples of localized fiber waviness observed both on the surface (IP waves) and through the thickness (OP waves).

Each discretized waveform's geometry was then mathematically characterized; cubic spline (Eq. 1) and sinusoidal curve (Eq. 2) fits were both evaluated for their applicability to mathematically describe the wave perturbation:

$$Y = Ax^3 + Bx^2 + Cx + D \tag{1}$$

$$Y = E + F\sin\left(\frac{2\pi}{\omega x + \varphi}\right), \tag{2}$$

where A, B, C, and D are polynomial coefficients, E is the offset, F is the amplitude, ω is the wavelength, and φ is the phase.

To optimize the goodness of fit of the wave spatial data to the mathematical formulations, a user-built least-squares regression algorithm was used. This function utilizes the generalized reduced gradient (GRG) constrained optimization algorithm. In a least-squares data fitting method, the most accurate model is established by minimization of the sum of squared residuals. A residual being the difference between an observed value and the fitted value provided by a mathematical model. The GRG algorithm was used to manipulate model values (A, B, C, D, E, F, ω, φ) until the sum of the squares was minimized (Biegler, 2011).

Both models, using spline and sinusoidal fits, yielded similar goodness-of-fit tendencies. The sinusoidal analysis proved to be faster and was utilized on bulk data analysis. Moreover, the ability to reference model parameters, which

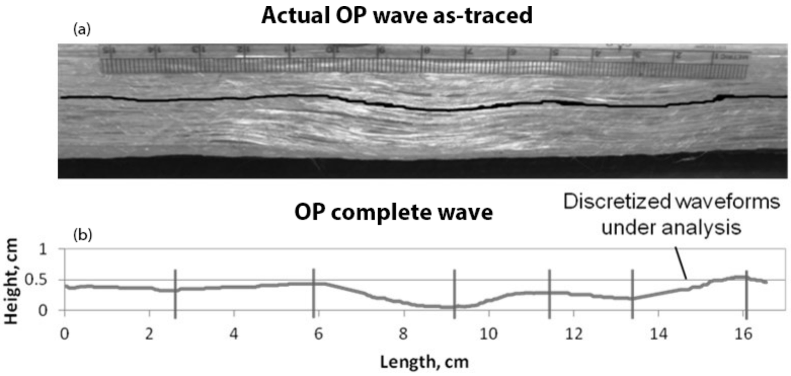

Figure 2. Example of OP waviness **(a)** with complete spatial data and discretization positions **(b)**.

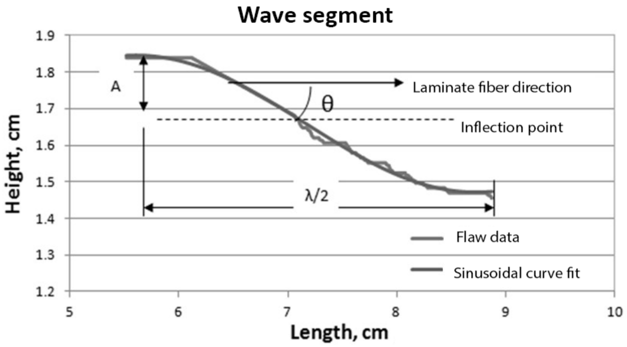

Figure 3. A sine wave superposed on a segment of the OP waviness shown in Fig. 2.

have a direct physical meaning (e.g., amplitude and wavelength), was useful in performing statistical characterization of wave parameters. Once a fit was performed, each wave segment was characterized in terms of wavelength, amplitude, and off-axis fiber angle, which is found by measuring the maximum misalignment angle of deviation from the intended fiber direction (Fig. 3). While previous studies have used aspect ratio or wave severity (amplitude / wavelength) instead of fiber angle as a metric for characterization, such quantification may be slightly more challenging in the field since the aspect ratio requires knowing both the amplitude and wavelength (Adams and Hyer, 1993; Adams and Bell, 1995; Mandell et al., 2003). Even though it is possible that only the fiber angle can be measured directly in the field, wave amplitude (A), wavelength (λ), and off-axis fiber angle (θ) were characterized, as shown in Fig. 3, for comparative purposes.

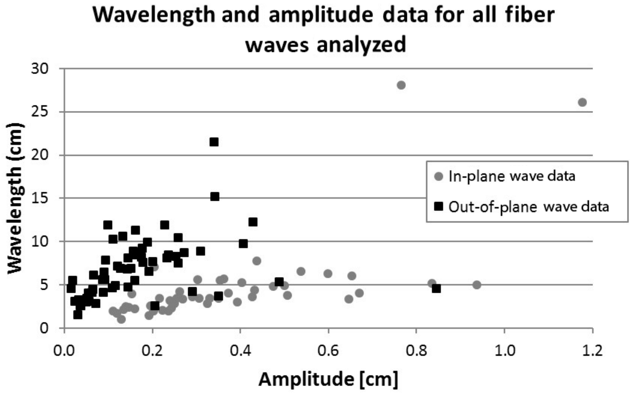

Figure 4. Collected OP and IP wave data (left to right, respectively).

Determination of defect parameters for testing

Characterization of the various wave flaws found in the field study yielded 63 OP and 48 IP independent, discrete waveforms (Nelson et al., 2012b). Values for amplitude and wavelength of each instance are shown in Fig. 4, where it may be seen that there is significant variability within the data. However, the data are well grouped, indicating consistency in the manufacturing processes. The resulting off-axis fiber angles from these OP and IP waves were collected and utilized as shown in Fig. 5. The reader should note that these angles were collected from blade sections that failed at these out-of-plane flaw locations, and, therefore, these magnitudes likely include plastic deformation.

Mean and standard deviation values were used to develop normal distributions to describe the frequency of flaw magnitude occurrences, and Weibull distributions (two parameter) were generated using maximum likelihood estimation. To develop frequency of occurrence distributions, the off-axis fiber angle values gathered from all wave segments were binned together into groups as shown in Fig. 5. For OP waves, angles were binned in 1° increments, while for IP waves, angles were binned in 4° increments. The frequency of each

Table 1. Summary of wave data generated from processes outlined in the text.

OP waves	Amplitude (cm)	Wavelength (cm)	Maximum fiber angle (°)
Min	0.02	1.58	0.6
Max	0.85	21.49	39.0
Mean	0.17	6.74	8.6
SD	0.11	3.00	2.8
IP waves	**Amplitude (cm)**	**Wavelength (cm)**	**Maximum fiber angle (°)**
Min	0.11	1.08	8.7
Max	1.18	28.12	50.7
Mean	0.37	4.75	26.7
SD	0.23	4.96	9.3

Table 2. OP and IP wave parameters as scaled for use in the coupon testing program.

Scaled OP waves	Amplitude (cm)	Wavelength (cm)	Maximum fiber angle (°)
OP1	0.29	2.28	36.8
OP2	0.07	0.54	34.8
OP3	0.07	0.23	8.6
Scaled IP waves	**Amplitude (cm)**	**Wavelength (cm)**	**Maximum fiber angle (°)**
IP1	0.45	2.38	48.9
IP2	0.19	1.00	47.8
IP3	0.19	2.38	24.8

fiber angle can be seen in Fig. 5 where the observed frequency of occurrence is displayed with applicable Weibull and normal distribution curves. In general, maximum wave fiber angle values show a strong inclination towards common distributions such as the Weibull and normal distributions for both cases with the normal distribution utilized throughout the probabilistic analysis. In general, these distributions were presented for completeness for working with probabilistic effects of defects and it is up to the user to decide which is the best case. Binning procedures were applied to amplitude and wavelength data for both wave types; however, the distributions were less accurate, further justifying characterization with fiber angle. Generalized information regarding both IP and OP wave group data is summarized in Table 1.

A test program focused on the characterization of the mechanical performance of specimens with scaled flaws was developed from the data collected in this study. Given the scale difference between the blades and coupon-sized test specimen, the flaws were scaled using a Weibull scaling analysis in which fracture strength was adjusted with material volume. Based on this "weakest link" theory, as material volume decreases, the population of defects also decreases, thereby reducing the probability of a failure from a flaw. The ratio of fracture strengths may then be found if the probability of survival is assumed to be the same for both small- and large-scale composite structures:

$$\frac{\sigma_1}{\sigma_2} = \left(\frac{V_2}{V_1}\right)^{\frac{1}{m}}, \tag{3}$$

where $\sigma_{1,2}$ is the fracture strengths $V_{1,2}$ is the volume, and m is the Weibull modulus. Comparisons were made between the coupons and as-built blade sections, utilizing the same length (coupon gauge length) and unit width. The four-ply laminate test specimen has a thickness of ~ 3.2 mm, which is 8.8 times smaller (volumetrically) than actual as-built sections. Using the volume fraction and a modulus of 29.1 in Eq. (3) (Wisnom, 1999), the Weibull scaling expression, it was found that the fracture strength for the larger as-built blade sections was expected to be approximately 7.1 % less than the coupons. To scale the as-built OP flaw waveforms, the mathematical description of each wave was integrated over the half wavelength to calculate the cross-sectional area bounded by each flaw curve. This was the only parameter needed as unit width was considered. The volumetric ratio between the full-scale blade sections and test specimen was then applied to the as-built flaw cross-sectional area. Knowing the scaled cross-sectional area, the amplitude and wavelength of each wave were solved for. It is important to note that this analysis was appropriate for the OP waves only. The IP waves did not vary with thickness, and therefore a volumetric scaling approach was not taken. Instead, each was scaled by the same ratio to fit within the coupon dimensions.

Using this method of scaling, three waveforms for each type of flaw were systematically chosen, as shown in Table 2, for testing based on geometry characterization and statistical significance while representing data points around an angular region of interest. The parameters for waves OP1 and OP2 were identified to be included due to the similarity in fiber angle occurring from a different combination of amplitude and wavelength. The additional OP wave (OP3) had mean values for all three parameters, and therefore landed in the center of all the parameter distributions. As such, these data points combined to sufficiently describe an OP wave common to the specific wind turbine application. The reader may note subtle variations in the mean values that result from the scaling process when compared to Table 1. By design, the mean value also delivered baseline values for comparison of the effects of amplitude and wavelength independently from the OP1 and OP2 results. IP test waves IP1 and IP2 followed the same approach as the OP in which they each had different amplitudes and wavelengths but resulted in similar misalignment angles. Similarly, the IP3 case represented the parametric mean for all values.

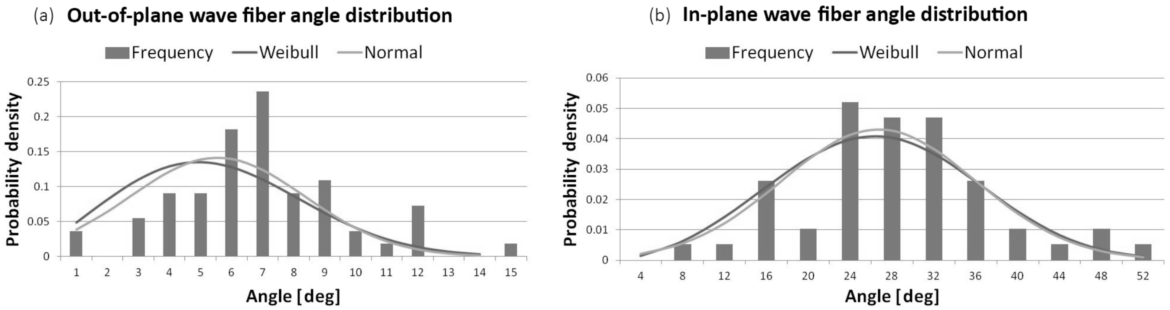

Figure 5. Distribution of all OP **(a)** and IP **(b)** wave fiber angles gathered.

3 Coupon manufacturing and methodology

All test coupons consisted of four-layer laminates infused utilizing a modified vacuum-assisted resin transfer molding (VARTM) process with a PPG-Devold 1250 $\mathrm{g\,m^{-2}}$ primarily unidirectional E-glass and a Hexion RIM 135 resin system. The nominal fiber volume fraction of the panels was 55 % with a nominal thickness of 0.8 mm for each layer resulting in a nominal total thickness of approximately 3.6 mm. Tensile coupons were cut to approximately 50 mm wide by 200 mm long and were tabbed, resulting in a gauge length of 100 mm. Compression coupons were cut to approximately 25 mm wide by 150 mm with gauge lengths of 25 or 38 mm depending on flaw wavelength.

Manufacturing processes were developed and utilized to create coupons with wavy fibers (Riddle et al., 2013; Nelson, 2013). IP waves were introduced by manually pulling the fibers transversely for one entire wavelength. OP waves, also for one entire wavelength, were created by placing discontinuous fibers transversely to build up the waveform. Due to variability in the specimen manufacturing processes, it was necessary to characterize the as-built flaw parameters prior to testing to ensure that all correlations were performed accurately. Through thickness, IP wave images for each layer were collected with the use of a computer tomography (CT) scanner in which wave parameters were measured as displayed in Fig. 6. OP waves were measured with the use of high-fidelity digital photographs in the same manner used to characterize the blade flaws above.

To measure the amount of porosity in the coupons, scanning electron microscopy (SEM) was used to image the cut surface plan (Fig. 7). Image processing techniques were then used to identify the location and size of gas inclusions and ultimately calculate the planar area fraction of porosity. This value was then extrapolated to percent porosity by volume. Burn-off testing was used to validate the percent porosity. However, this technique yields no indication of size or location of inclusion; therefore, it was not employed for data collection. Given the difficulty in testing and the destructive nature of this method, alternative methods including radiodensity, which has shown promising results, continue to be investigated (Shapurian et al., 2006).

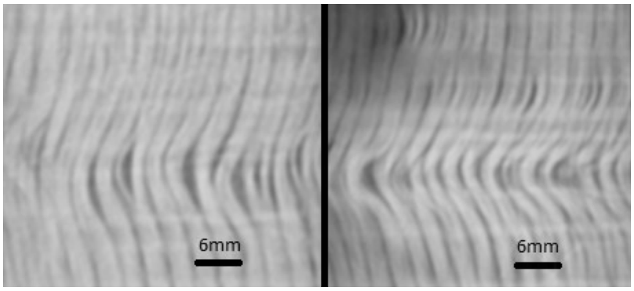

Figure 6. Radiographic images of IP waves found on different layers of one specimen.

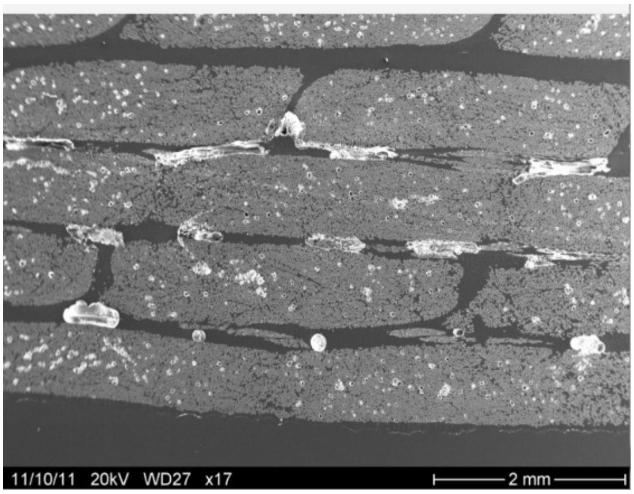

Figure 7. Cross-section SEM image of a coupon containing porosity.

Quasi-static, displacement-controlled ramp tests on all specimens were conducted at a rate of 0.05 $\mathrm{mm\,s^{-1}}$ in tension and 0.45 $\mathrm{mm\,s^{-1}}$ in compression for all four-ply coupons. These tensile tests were performed based on the ASTM D3039 tensile testing of composites standard (ASTM D3039, 2014). Compression testing was more

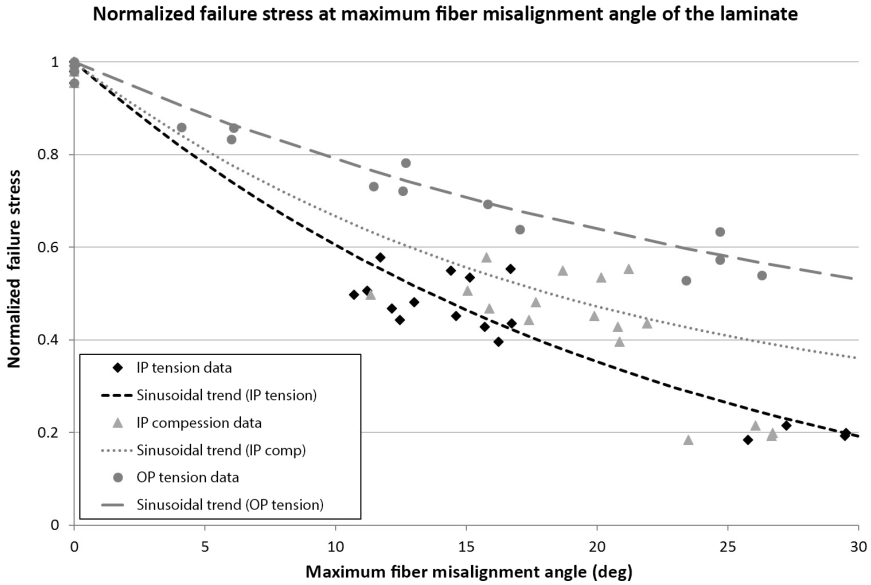

Figure 8. Peak stress of OP and IP waves at various fiber angles (left to right, respectively).

loosely based on ASTM D3410 and D6641 (ASTM D3410, 2016; ASTM D6641, 2016). Digital image correlation (DIC) was utilized to capture displacement and full-field strain.

Material properties were calculated for each coupon and then averaged for each group. Where bending was found to be minimal enough to be disregarded, ultimate tensile or compressive strength was calculated:

$$F^{\mathrm{tu}} = P^{\max}/A, \tag{4}$$

where F^{tu} is the ultimate tensile or compressive strength, $P^{\max}$ is the maximum load before failure, and A is the average cross-sectional area. This equation was modified to calculate the stress at each point (σ_i), necessary for plotting of stress–strain curves, by substituting P_i, the load at the ith point, for $P^{\max}$. Similarly, ultimate shear strength was calculated for ±45° specimen:

$$\tau_{12}^{\mathrm{tu}} = P^{\max}/2A, \tag{5}$$

where τ_{12}^{tu} is maximum IP shear.

Strain was calculated utilizing a DIC system based on the full field of the coupon such that it was calculated for the entire gauge section. To ensure a consistent method that would allow for the calculation of both unflawed controls and flawed specimens, strain was generalized for the entire gauge length, which was the same for all coupons. This allowed for consistent comparison given the different flaws, specifically the variation in fiber misalignment angles.

Once both stress and strain were calculated, modulus of elasticity (E) was calculated for each specimen utilizing this data. Initial linear portions of each stress–strain curve (generally 0.1–0.3 % strain) were chosen to ensure accuracy and consistency of the chord modulus utilized:

$$E = \Delta\sigma/\Delta\epsilon. \tag{6}$$

4 Results and discussion

4.1 Effects of defect trends

The goal of establishing benchmark material and flaw testing based on in situ defect parameters to contribute to accurate prediction of the effects of defects in thicker laminates such as those found in wind turbine blades was achieved. By assessing typical defects found in wind turbine blades, defects were discretized, measured, and scaled into coupon testing.

4.1.1 IP and OP wave trends

The results of failure stress versus maximum fiber misalignment angle for IP and OP waves are shown in Fig. 8. These results show that strength degradation in laminates with waves tends to correlate well with the average of the maximum fiber misalignment angles of all layers in the laminate as measured through the thickness. An alternative correlation using the single maximum fiber angle can be achieved with a minor reduction in accuracy. For example, an OP wave embedded in a planar structure under compression is predominately prone to buckling due to the inherent eccentricity. While buckling is a common mode of failure in a wind turbine blade, it is driven predominately by the global structure and local geometry effects. Thus, even with the use of symmetric OP waves to reduce buckling during coupon testing, the reduction in material property in a compressed section of a blade is likely to have a more complex effect. As such, no OP wave data are presented due to coupon testing.

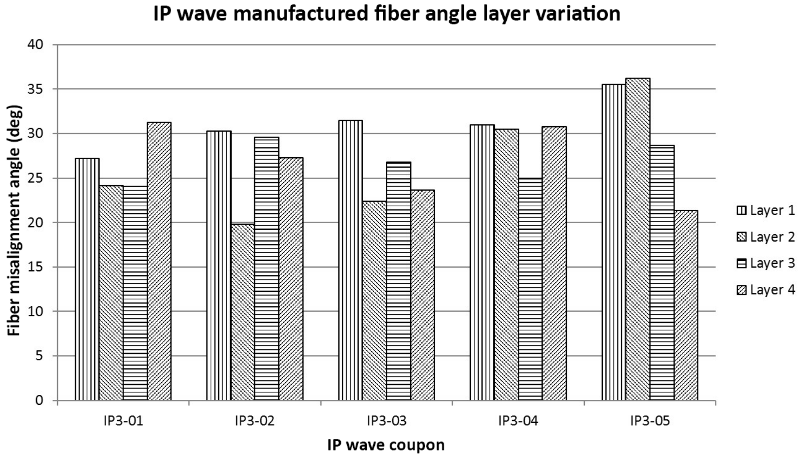

Figure 9. Examples of layer-by-layer fiber wave variation.

Linear regression analysis demonstrated that all the data displayed in Fig. 8 fit best to exponentially decaying sinusoidal functions found by optimizing the coefficient of determination. This fit has roots from strength of materials failure criteria in which for an off-axis ply, the stresses rotate per

$$\sigma'_{ij} = a_{ik} a_{jl} \sigma_{kl}, \tag{7}$$

where σ'_{ij} is the rotated local stress, σ_{kl} is the global stress, and a_{ik} and a_{jl} are direction cosines of the rotated region. With an interactive failure criterion, such as Tsai–Wu, the failure curve versus off-axis angle is essentially a decaying stress rotation function that starts with fiber-dominated failure and quickly transitions to matrix-dominated failure with off-axis loading (Barbero, 2011). Based on these results, this type of analysis can be used to quickly assess the tension and compression failure strengths of wavy materials.

Due to variability in the specimen manufacturing processes, it was necessary to characterize the as-built flaw parameters prior to testing to ensure that all correlations were performed accurately. Through thickness, IP wave images for each layer were collected with the use of a CT scanner in which wave parameters were measured as displayed in Fig. 6. For the case of IP waves, each layer's off-axis fiber angle was recorded and examples of the layer-by-layer variation in fiber angle are given in Fig. 9. Once testing of the IP wave samples was completed, the results were reviewed for correlation to the maximum and average, through thickness wave angle. The analysis revealed very similar correlation traits, particularly when the maximum wave angle was considered, making it the characteristic parameter used to describe as-built flaw magnitudes. Further, partners in the BRC suggested that using the maximum angle would fit more easily within a quality plan. OP waves were measured with the use of high-fidelity digital photographs, and little migration during manufacturing was noted.

4.1.2 Porosity trends

Test specimens in the investigation have been manufactured using a vacuum bag technique; therefore, it is necessary to include volume effects. A simple method for comparing results in this case is to normalize the failure stresses to 55 % fiber volume ratio, V_f. Figure 10 shows a comparison between porosity content and the reduced strength. The void content was determined using image analysis of specimens from the same plates that were used for the test coupons. The void data are presented as a function of void content in the composite to provide use to designers on that basis. Some discussion on the micromechanics of voids in the composite is warranted. The influence of voids on the mechanical properties has the effect of reducing the bulk modulus of the resin. While this does not have as great of an effect on tension, the reduced modulus has a significant effect for compression strength as the reduced modulus does not support the fibers in compression as well as a stiffer matrix. While the results shown in Fig. 10 are for an expected range, the entire data set was compared with similar data from a prominent blade manufacturer with strong correlation between the two data sets (Fig. 10) (TPI-RI Materials Testing Lab, 2010). Based on these results, the BRC decided to set 2 % porosity as the upper threshold for acceptable porosity in blades. As such, further analysis was focused on this worst-case upper bound.

4.2 Comparison of material properties

Material properties for each coupon were calculated and averaged for each flaw group and are shown in Tables 3 and 4 with standard deviations included for ultimate stress to indicate the distribution size of the coupons tested for each defect type. It is important to note that the 2 % porosity case was used because the BRC set this as the threshold of acceptable porosity. To ensure accuracy of these values, com-

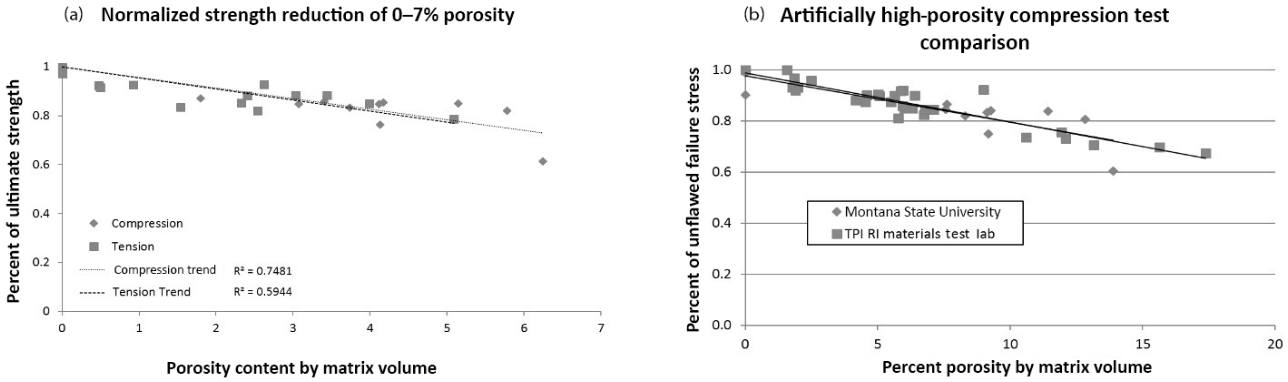

Figure 10. Reduction in strength due to porosity in the 0 to 7 % porosity range and comparison with the high-porosity blade manufacturer data set **(b)**.

parisons were made between the control results and the results of similar tests published in the Montana State University Composite Material Database (Table 5). Modulus of elasticity and maximum strain were chosen as points of comparison as they were critical for analytical inputs and correlation. These comparisons indicated that while the material properties compare acceptably for tension, the compressive failure strains for the test group appeared less accurate. This was likely due to the unrestrained method of testing in compression, which resulted in bending and buckling. However, much less bending was noted in the flawed specimen, apart from OP waves. The lack of bending prior to failure indicated that damage occurred at the flawed area prior to bending occurring, suggesting that these data were acceptable.

4.2.1 IP wave analysis

Ultimate stress values for the each of the 0° IP wave groups tested in tension were found to have a significant decrease in ultimate stress: from 54 down to 25 % of the control for the IP waves. As noted in Table 2, the amplitude and wavelengths for each of these waves varied, and even though IP3 had the highest ultimate stress, it also had the largest wavelength. Furthermore, IP1 had a larger amplitude and wavelength than IP2, while the ultimate stress for each was approximately the same. Based on previous research, similarity of the results was expected between the IP1 and IP2 groups, as the fiber angles were similar in the two groups.

It is also interesting to note that the stiffness for these groups was 85–96 % of the control. Initial stiffness was similar to the control; however, the ultimate stresses and strains were notably lower. This was likely due to the load matrix "locking" the fibers into place at the ends of each wave before the matrix cracking noted above. Very similar results and trends were also noted for the 0° IP wave groups tested in compression. Overall, IP waves resulted in reduced material properties when included in 0° laminates.

The ±45° groups tested in tension were noted to have a similar damage progression as the 0° wave groups as noted in ultimate stress values very similar to the control group (96–98 % of control), and the strains at failure were found to be relatively consistent with the control (92–112 %). Of note was the stiffness increase compared to the control group (103–115 %), likely for the same reasons given for the 0° IP groups noted above, which resulted in significantly lower values for the Poisson's ratio. The ±45° compression results were rather remarkable, as the ultimate stress for all IP wave groups was significantly higher compared to similar control groups (127–185 %) even though strains at failure were lower (48–52 %). This resulted in significantly stiffer ±45° laminates, causing a negative Poisson's ratio for the IP wave groups in compression. These results are due to the increased load-carrying ability of the laminates caused by the fibers in the wave approaching 0°. However, both IP1 and IP2 had the same fiber angle, though the ultimate stresses in each were different: 181 and 139 MPa, respectively. This difference may be from differences between initial imparted and as-manufactured amplitudes, wavelengths, fiber angles, and the fiber content of the final laminate as noted above. In short, while properties decreased in 0° laminates including IP waves, laminates including ±45° performed as well or better than control, eliminating the need for further analysis. In addition, these data offer reasonable convergence points for the analytical modeling efforts.

Damage progression was found to vary for each wave type, but was observed to generally involve matrix cracking, fiber failure, and ply delamination often before load redistribution up to, ultimately, failure. Damage progression of the IP waves, as shown for a representative case in Fig. 11, was directly influenced by the flaw. It is apparent in the images associated with each identified full-field average strain that damage occurs around the wave. With the aid of the DIC, it was noted that the strain accumulated in the wave area, progressing transversely from the angled fiber toward the peak of the wave as seen in the 1.1 % strain compared to the 1.5 %

Table 3. Static properties for laminates tested in tension and calculated percentage of control laminates.

Tension	Control		Porosity		IP1		IP2		IP3		OP1		OP2		OP3	
	0°	±45°	0°	±45°	0°	±45°	0°	±45°	0°	±45°	0°	±45°	0°	±45°	0°	±45°
Ultimate stress (MPa)	990	112	950	103	344	109	226	107	521	108	417	84	742	101	752	102
SD	(40)	(2.0)	(19)	(1.5)	(43)	(1.1)	(24)	(4.1)	(24)	(4.1)	(26)	(5.3)	(79)	(2.2)	(43)	(2.8)
% control	–	–	96 %	93 %	35 %	98 %	23 %	96 %	53 %	97 %	42 %	75 %	75 %	91 %	76 %	91 %
Strain at failure (%)	2.64 %	1.44 %	2.54 %	1.30 %	1.66 %	1.72 %	1.66 %	2.02 %	1.66 %	1.13 %	4.77 %	4.91 %	4.92 %	3.06 %	4.56 %	3.43 %
% control	–	–	96 %	90 %	63 %	119 %	63 %	140 %	63 %	78 %	181 %	341 %	186 %	213 %	173 %	238 %
Est. modulus of elasticity (GPa)	41.1	16.2	39.6	16.6	34.8	16.8	24.1	16.6	39.6	18.7	17.3	5.9	32.1	16.7	31.2	15.3
% control	–	–	96 %	103 %	85 %	104 %	59 %	102 %	96 %	115 %	42 %	36 %	78 %	103 %	76 %	94 %
Poisson's ratio	0.27		–		–		–		–		–		–		–	

Table 4. Static properties for laminates tested in compression and calculated percentage of control laminates.

Compression	Control		Porosity		IP1		IP2		IP3		OP 1		OP 2A		OP 4A	
	0°	±45°	0°	±45°	0°	±45°	0°	±45°	0°	±45°	0°	±45°	0°	±45°	0°	±45°
Ultimate stress (MPa)	582	124	491	125	216	181	216	139	257	165	95	43	227	90	207	86
SD	(28)	(1.2)	(20)	(1.5)	(10)	(5.0)	(9.0)	(3.0)	(23)	(2.8)	(13)	(2.1)	(3.4)	(7.5)	(5.7)	(0.78)
% control	–	–	84 %	101 %	37 %	147 %	37 %	112 %	44 %	133 %	16 %	35 %	39 %	72 %	36 %	70 %
Strain at failure (%)	1.76 %	1.16 %	1.44 %	1.06 %	0.84 %	0.51 %	0.91 %	0.82 %	0.84 %	0.59 %	0.71 %	1.11 %	1.04 %	0.93 %	0.92 %	0.84 %
% control	–	–	82 %	91 %	48 %	44 %	52 %	71 %	48 %	51 %	40 %	96 %	59 %	81 %	52 %	72 %
Est. modulus of elasticity (GPa)	37.2	15.5	36.5	16.4	31.0	28.7	29.5	19.7	34.3	25.4	12.4	4.5	23.0	12.4	23.3	12.0
% control	–	–	98 %	106 %	83 %	185 %	79 %	127 %	92 %	164 %	33 %	29 %	62 %	80 %	63 %	77 %
Poisson's ratio	0.28		–		–		–		–		–		–		–	

Table 5. Comparison of control test results to published MSU composite database results in tension and compression.

Test	Tension				Compression			
Material orientation	0°		45°		0°		45°	
Data source	Database	Testing	Database	Testing	Database	Testing	Database	Testing
Modulus of elasticity (GPa)	41.1	40.6	14.9	16.2	38.4*	37.2	14.4*	15.5
Strain at failure (%)	2.7	2.6	2.9*	2.6	2.4	1.8	1.6	1.6

* Indicates that an exact material match was not available and a similar material system was used instead.

strain DIC images. Fiber breakage appeared to initiate at the point at which the strain accumulations from each side of the wave met, as seen in the 2 % strain DIC image. These observations combined with the strains at failure indicate that damage accumulation was at lower strains than the control group and was the result of shear softening leading to shear failure around the wave. Similar responses were noted for compression and the other IP wave cases.

In summary, it should be noted that the IP3 case had decreases in material strength, and significant degradation was noted, making the result that this case was optimal for baseline use for modeling efforts (Riddle et al., 2017; Nelson et al., 2017). Further, it was decided that since this case had a fiber misalignment angle close to 30°, it would be a good median case for these endeavors. The resulting stress–strain curves, utilizing the DIC data from this test group, for this IP wave case in tension and compression are found in Fig. 12. Data beyond failure and maximum stress were gathered to begin to establish a comprehensive understanding of the material to be applied to future work with larger substructures and structures. As such, this geometry and these results were utilized as the baseline model for experimental and analytical correlation of each modeling type outlined below.

4.2.2 OP wave analysis

Test results for the OP wave groups are also noted in Tables 2 and 3 with a representative stress–strain response shown in Fig. 13. Results from test observation and the DIC suggest that each of the OP wave groups was noted to have similar damage progression in tension compared to IP waves in which delamination took the place of the matrix damage between the fiber tows. As strain levels increased, cracks initiated in the resin between the layers at the ends of the wave before delaminating. However, unlike the behavior of IP waves, after delamination and significant fiber straightening, the failure area for the OP wave specimens was concentrated at the peak area of the wave. This was due to the fibers being pulled straight and the center of bending being at the peak of the wave. Due to the eccentricity, compression testing of the OP waves was difficult due to large wavelengths creating a long, unsupported gauge length, resulting in bending and ultimately buckling. As such, significant decreases in calculated moduli of elasticity, ultimate strength, and strain at failure were noted and results were considered unusable for correlation given these responses.

It must be noted that the waveforms for the entire OP1 group delaminated during testing. This resulted in an extreme decrease in the ultimate stress and stiffness results of the OP1 groups in both tension and compression. As such, OP1 was deemed unusable for correlation in both tension and compression. The two other cases, OP2 and OP3, were found to have a more consistent response. Ultimate stress and strain at failure values for the OP2 and OP3 0 and ±45° tension groups were decreased compared to the control but were increased compared to the IP waves. Thus, moduli of elasticity values were similar to the control due to load being transferred more consistently through the wave than seen with IP waves due to the configuration described above. Given the consistency of these waves in tension, the OP3 case was utilized for correlation. Overall, the static testing performed allowed for initial analysis while determining convergence points for analytical models.

5 Conclusions and future work

Using this consistent framework that was established and validated, defects common to wind turbine blades have been quantified. To effectively characterize, categorize, and analyze defects, the framework requires accurate data collection following consistent scientific procedures. This provides an unambiguous benchmark set of data to compare to more random, as-manufactured defects. With proper characterization, it is possible to establish the mechanical response of a flaw using laboratory testing. Results from static testing indicate that there is a strong correlation between flaw parameters and mechanical response. Since the flaws went across the entire width of the sample, applying these knockdowns directly is conservative, but may not be realistic, especially if the surrounding material in a blade structure can redistribute loads from local failures. Going forward, the characterization techniques described herein may be applied to incoming data and will enable the generation of a statistically significant and comprehensive flaw database.

This work provides a sound starting point, but only constitutes the building blocks for a comprehensive reliability pro-

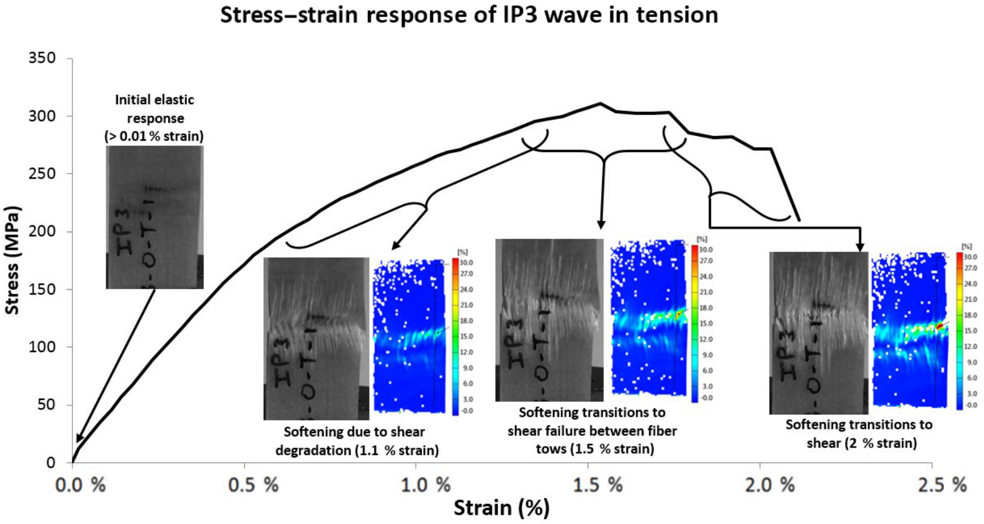

Figure 11. Stress–strain response of IP3 wave coupon shown at increasing average full field strain with associated DIC strain fields identifying damage progression.

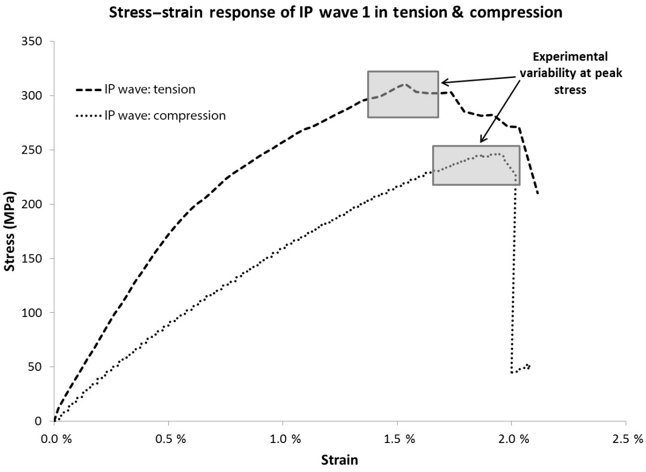

Figure 12. Stress–strain of IP wave 3 in tension and compression utilized for baseline model correlations with associated experimental variability.

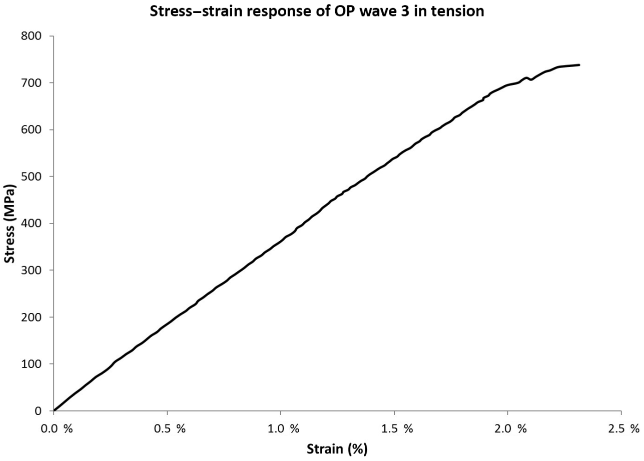

Figure 13. Stress–strain of OP wave 3 in tension utilized for initial OP wave model correlations.

gram aimed at reducing failures as a result of defects. Since reliability estimation is inadequate for composite structures due to the uncertainties, a probabilistic approach is required to achieve an acceptable level of confidence. This approach must consider multi-scale mechanical property variability, damage and defect detection, damage progression, residual strength analysis, and global and macro structural response.

Using the metrics developed herein to precisely address the geometric nature of flaws based on statistical commonality in blades, mechanical testing and probabilistic modeling were performed. The work herein led to the establishment of a consistent framework that was validated for quantitative categorization and analysis of flaws to predict blade failure. Further, this significant coupon-level testing effort has determined material properties and characterized damage progression in both flawed and unflawed specimens, allowing for baseline comparisons of the modeling methods. In short, these data allowed for direct comparison in determination of the consistency, accuracy, and predictive capability of each modeling approach.

Data availability. Data may be found as reported to Sandia National Laboratories in Nelson et al. (2012a, b). In addition, data have also been added to the Blade Materials & Structures Testing Database compiled by the Composite Technologies Research Group at Montana State University and the database is updated and hosted by Sandia National, http://energy.sandia.gov/energy/renewable-energy/water-power/technology-development/advanced-materials/mhk-materials-database/.

Competing interests. The authors declare that they have no conflict of interest.

Acknowledgements. The authors wish to acknowledge the help from Sandia contract monitors Joshua Paquette and Daniel Laird. The authors also wish to acknowledge technical help from Tom Ashwill and Mark Rumsey. In addition, the work and research presented herein could not have been performed without the assistance of the entire Montana State University Composite Technologies Research Group.

Edited by: Lars Pilgaard Mikkelsen
Reviewed by: two anonymous referees

References

Adams, D. O. and Bell, S. J.: Compression strength reductions in composite laminates due to multiple-layer waviness, Compos. Sci. Technol., 53, 207–212, https://doi.org/10.1016/0266-3538(95)00020-8, 1995.

Adams, D. O. and Hyer, M.: Effects of layer waviness on the compression strength of thermoplastic composite laminates, J. Reinf. Plast. Comp., 12, 414–429, https://doi.org/10.1177/073168449301200404, 1993.

ASTM D3039/D3039M-14: Standard Test Method for Tensile Properties of Polymer Matrix Composite Materials, ASTM International, https://doi.org/10.1520/D3039_D3039M-14, 2014.

ASTM D3410/D3410M-16: Standard Test Method for Compressive Properties of Polymer Matrix Composite Materials with Unsupported Gage Section by Shear Loading, ASTM International, https://doi.org/10.1520/D3410_D3410M-16, 2016.

ASTM D6641/D6641M-16e1: Standard Test Method for Compressive Properties of Polymer Matrix Composite Materials Using a Combined Loading Compression (CLC) Test Fixture, ASTM International, https://doi.org/10.1520/D6641_D6641M-16E01, 2016.

Barbero, E. J.: Introduction to Composite Materials Design, 1st Edn., CRC Press, Boca Raton, FL, USA, 2011.

Biegler, L. T.: Nonlinear Programming: Concepts and Algorithms for Process Optimization, Pittsburgh: Carnegie Mellon, CAPD Center, 2011.

Hill, R. R., Peters, V. A., Stinebaugh, V. A., and Veers, P. S.: Wind Turbine Reliability Database Update, Sandia Report SAND2009-1171, 2009.

Mandell, J., Samborsky, D., Wang, L., and Wahl, N., New fatigue data for wind turbine blade materials, AIAA SDM Conference, 41st Aerospace Sciences Meeting and Exhibit, Reno, Nevada, organized by American Institute of Aeronautics and Astronautics, https://doi.org/10.2514/6.2003-692, 2003.

Nelson, J. W.: A comparison of continuum and discrete modelling techniques of the effects of manufacturing defects common to composite structures, PhD Thesis, Montana State University, 2013.

Nelson, J., Riddle, T., and Cairns, D.: Effects of defects in composite wind turbine blades: Round 1, available at: http://prod.sandia.gov/techlib/access-control.cgi/2012/128110.pdf (last access: 2 December 2017), 2012a.

Nelson, J., Riddle, T., and Cairns, D.: Effects of defects in composite wind turbine blades: Round 2, available at: http://prod.sandia.gov/techlib/access-control.cgi/2012/128111.pdf (last access: 2 December 2017), 2012b.

Nelson, J. W., Riddle, T. W., and Cairns, D. S.: Effects of defects in composite wind turbine blades – Part 2: Progressive damage modeling of fiberglass-reinforced epoxy composites with manufacturing-induced waves, Wind Energ. Sci., 2, 653–669, https://doi.org/10.5194/wes-2-653-2017, 2017.

Red, C.: Wind turbine blades: Big and getting bigger, Composites Technology, June, Denver, CO, USA, 2008.

Riddle, T. W., Nelson, J. W., and Cairns, D. S.: Probabilistic Design of Wind Turbine Blades with Treatment of Manufacturing Defects as Uncertainty Variables in a Framework, Wind Energ. Sci. Discuss., https://doi.org/10.5194/wes-2017-14, in review, 2017.

Riddle, W. W.: Development of reliability program for risk assessment of composite structures treating defects as uncertainty variables, PhD Thesis, Montana State University, 2013.

Roach, D., Rackow, K., and Duvall, R., Addressing the need for non-destructive inspection of wind turbine blades, Wind Turbine Blade Workshop, Sandia National Labs, Albuquerque, NM, USA, 2010.

Shapurian, T., Damoulis, P. D., Reiser, G. M., Griffin, T. J., and Rand, W. M.: Quantitative evaluation of bone density using the Hounsfield index, Int. J. Oral Max. Impl., 21, 290–298, 2006.

TPI-RI Materials Testing Lab: Compressive Testing of Specimens with Artifically High Void Content, TPI Composites Inc, Warren, RI, USA, Doc. No. 10022, 2010.

Veldkamp, D.: A Probabilistic Evaluation of Wind Turbine Fatigue Design Rules, Wind Energy, 11, 655–672, https://doi.org/10.1002/we.287, 2008.

Walford, C. A.: Wind Turbine Reliability: Understanding and Minimizing Wind Turbine Operation and Maintenance Costs, Sandia Report SAND2006-1100, Sandia National Laboratory, Albuquerque, NM, USA, 2008.

Wisnom, M. R.: Size effects in the testing of fibre-composite materials, Compo. Sci. Technol., 59, 1937–1957, https://doi.org/10.1016/s0266-3538(99)00053-6, 1999.